1   **Shallow Slow Earthquake Episodes Near the Trench Axis Off Costa Rica**

2

3   **Satoru Baba[1], Kazushige Obara[1], Shunsuke Takemura[1], Akiko Takeo[1], and Geoffrey A.**
4   **Abers[2]**

5   [1]Earthquake Research Institute, The University of Tokyo, Tokyo, Japan

6   [2]Department of Earth and Atmospheric Sciences, Cornell University, Ithaca, New York, United
7   States of America

8

9   Corresponding author: Satoru Baba (babasatoru@eri.u-tokyo.ac.jp)

10

11   **Key Points:**

12   •   Shallow very low frequency earthquakes (VLFEs) and tremors are detected off Costa
13   Rica near the Middle America Trench

14   •   Distribution of VLFEs and tremors is spatially correlated with slow slip events

15   •   Scaled energy of shallow slow earthquakes off Costa Rica is 10^{-9}–10^{-8}, which is similar to
16   those in Nankai

17

18 **Abstract**

19   Slow earthquakes are mainly distributed in regions surrounding seismogenic zones
20 along the plate boundaries of subduction zones. In the Central American subduction zone, large
21 regular interplate earthquakes with magnitudes of 7–8 occur repeatedly around the Nicoya
22 Peninsula, in Costa Rica, and a tsunami earthquake occurred off Nicaragua, just north of Costa
23 Rica, in 1992. To clarify the spatial distribution of various slip behaviors at the plate boundary, we
24 detected and located very low frequency earthquakes (VLFEs) around the Nicoya Peninsula using
25 a grid-search matched-filter technique with synthetic templates based on a regional three-
26 dimensional model. VLFEs were active in September 2004 and August 2005, mainly near the
27 trench axis, updip of the seismogenic zone. The distribution of VLFEs overlapped with large slip
28 areas of slow slip events. Low frequency tremor signals were also found in high-frequency
29 seismogram envelopes within the same time windows as detected VLFEs; thus, we also
30 investigated the energy rates of tremors accompanied by VLFEs. The range of scaled energy,
31 which is the ratio of the seismic energy rate of a tremor to the seismic moment rate of
32 accompanying VLFE and related to the rupture process of seismic phenomena, was 10^{-9}–10^{-8}. The
33 along-dip separation of shallow slow and large earthquakes and the range of the scaled energy off
34 Costa Rica are similar to those in shallow slow earthquakes in Nankai, which shares a similar
35 thermal structure along the shallow plate boundary.

36 **Plain language summary**

37   Slow earthquakes generally occur on the plate boundaries of subduction zones. We
38 detected and located very low frequency earthquakes (VLFEs), which are a type of slow
39 earthquake, off Costa Rica. The VLFEs occurred at a depth range of 6–10 km, and their spatial
40 distribution is correlated with slow slip events, another type of slow earthquakes. The spatial
41 separation of slow and large regular earthquakes is common to the Nankai subduction zone. Low
42 frequency tremor signals, which are also classified as slow earthquakes, were also found in
43 seismograms at higher frequencies within the same time windows of detected VLFEs. We also
44 estimated the ratio of energy rates of tremors to moment rates of VLFEs, which relates to the
45 rupture process of seismic phenomena. The ratio is 10^{-9}–10^{-8} off Costa Rica, similar to that in
46 shallow slow earthquakes in the Nankai subduction zone.

47 **1. Introduction**

48   Slow earthquakes are mainly observed in regions surrounding seismogenic zones, which
49 are the areas that rupture in large regular earthquakes, along the plate boundaries of subduction
50 zones (e.g., Obara & Kato, 2016) or strike-slip faults (e.g., Nadeau & Dolenc, 2005; Wang &
51 Barbot, 2020). Various types of slow earthquakes, such as low frequency tremors (tectonic
52 tremors; e.g., Obara, 2002), low frequency earthquakes (LFEs; e.g., Shelly et al., 2006), very low
53 frequency earthquakes (VLFEs; e.g., Obara & Ito, 2005), and slow slip events (SSEs; e.g., Dragert
54 et al., 2001) have been observed in many subduction zones. Although there are areas where some
55 types of slow earthquakes are not spatiotemporally correspondent (Hutchison, 2020; Hutchison &
56 Ghosh, 2016, 2019), they often correlate spatiotemporally, which is termed episodic tremor and
57 slip (ETS). ETSs were observed in deep Cascadia (e.g., Ghosh et al., 2015; Rogers & Dragert,
58 2003) and deep Nankai (e.g., Ito et al., 2007; Obara, 2011), for example. Recently, in the Nankai
59 subduction zone, pore fluid pressure changes have been observed during tremor and VLFE
60 activities and are considered to reflect shallow SSEs by offshore borehole observations (Araki et

61 al., 2017; Nakano et al., 2018). The hypocenters and focal mechanisms of slow earthquakes are
62 generally consistent with shear slip on the plate boundaries. VLFE episodes and SSEs occur in
63 almost identical source regions and their temporal changes of moment release are similar during
64 an ETS, therefore VLFE episodes are considered as proxies for SSEs (Hutchison & Ghosh, 2019;
65 Ito et al., 2007; Nakano et al., 2018; Yokota & Ishikawa, 2020). In summary, the distribution of
66 slow earthquakes is related to large earthquake slip areas, interplate coupling, or fluid distribution
67 (e.g., Baba et al., 2020b; Ghosh et al., 2015; Obara & Kato, 2016).

68   In the Central American subduction zone, the Cocos plate subducts beneath the Caribbean
69 plate at the Middle America Trench at a rate of approximately 80 mm/year (Figure 1b; referred
70 from NUVEL1A; DeMets et al., 1994). In this subduction zone, large thrust-type earthquakes with
71 a moment magnitude (M_W) of 7–8 occur with a recurrence interval of tens of years around the
72 Nicoya Peninsula, in Costa Rica (light blue areas in Figure 1a; Protti, 1995; Yue et al., 2013). The
73 coseismic slip areas of these large earthquakes are distributed at a depth range of 10–35 km beneath
74 the peninsula and off the coast. The latest large earthquake with M_W of 7.6 occurred on 5
75 September, 2012 (green contour lines in Figure 1a; Yue et al., 2013). In the vicinity, a tsunami
76 earthquake with M_W of 7.6 also occurred off Nicaragua, just north of Costa Rica, on 2 September,
77 1992 (dark blue area in Figure 1a; Satake, 1994).

78   In addition to large regular and tsunami earthquakes, slow earthquakes also occur around
79 the Nicoya Peninsula. The Global Navigation Satellite System data revealed that SSEs with M_W
80 of 6.6–7.2 occur at intervals of 21.7±2.6 months (Jiang et al., 2012; Xie et al., 2020). The large
81 slip area of the SSE in 2007 was separated into downdip and updip areas by the seismogenic slip
82 area (Jiang et al., 2012, 2017; Outerbridge et al., 2010). The spatiotemporal change in relation to
83 the 2012 M_W 7.6 earthquake was investigated by previous studies (Dixon et al., 2014; Voss et al.,
84 2017), and an SSE preceded the 2012 M_W 7.6 earthquake (Voss et al., 2018) in the almost same
85 area of the 2007 SSE, similar to both the slow slip before the 2011 Tohoku earthquake in Japan
86 (Ito et al., 2013; Kato et al., 2012) and the slow slip before the 2014 Iquique earthquake in Chile
87 (Kato & Nakagawa, 2014; Ruiz et al., 2017).

88   By using high-frequency (>1 Hz) seismograms, Brown et al. (2009) and Outerbridge et al.
89 (2010) located LFEs and tremors in 2007, respectively (Figure 1a). The tremors and LFEs were
90 located in almost the same area, downdip of the seismogenic zone. Although tremors and LFEs
91 were temporally correlated with the SSE, the location of tremors and LFEs were separated from
92 the large slip area of the 2007 SSE. On the other hand, Walter et al. (2011) located many tremors
93 in the offshore region from 2007 to 2009. Walter et al. (2013) also found that VLFEs appeared in
94 seismograms in a frequency range of 0.02–0.05 Hz and were temporally correlated with tremors
95 in the time period of the 2008 SSE. Based on beamforming analysis, they estimated the propagation
96 direction and the propagation speed of VLFE signals and suggested that VLFEs also occurred in
97 offshore areas. Due to the limitations of a conventional analysis, however, epicenters of VLFEs in
98 offshore areas were not located. Therefore, the detailed spatial distribution of VLFEs off Costa
99 Rica is still not well understood.

100   The spatial variation of slow and large regular earthquakes can reflect the spatial
101 heterogeneity of the frictional conditions on the plate boundary (e.g., Baba et al., 2020b). To clarify
102 the spatial relationship between slow and large regular earthquake distribution around the Nicoya
103 Peninsula, an accurate spatial distribution of VLFEs is needed. Thus, we detected VLFEs around
104 the Nicoya Peninsula using a temporary broadband seismic network from August 2004 to January
105 2006 because signals of VLFEs are less attenuated than those of tremors and propagate longer

106   distances. The method is based on the matched-filter technique. Template waveforms from
107   possible VLFE locations were evaluated by numerical simulations of seismic wave propagation
108   using a regional three-dimensional (3D) velocity structure model. In addition, scaled energy is an
109   informative parameter for the rupture process of seismic phenomena (Kanamori & Rivera, 2006).
110   Although scaled energies of slow earthquakes around Japan were well investigated by previous
111   studies (e.g., Ide & Yabe, 2014; Yabe et al., 2019; 2021), those in Costa Rica was not estimated.
112   Therefore, we also estimated the seismic energy rate functions of tremors accompanied by VLFEs
113   by using high frequency (2–8 Hz) seismograms to evaluate the scaled energy of slow earthquakes
114   around the Nicoya Peninsula.

115   2. VLFE analysis

116   2.1. Data and method
117   2.1.1. Data

118   We used waveforms of a temporary seismic network, Tomography Under Costa Rica and
119   Nicaragua (TUCAN; Abers & Fischer, 2003), recorded from August 2004 to January 2006. There
120   were 49 broadband seismic stations in four lines (Figure 1b). For the VLFE analysis, we used 14
121   stations near the Nicoya Peninsula in Costa Rica (shown in Figure 1a), because signals of VLFEs
122   are relatively clear in these 14 stations and using all stations causes higher computational cost for
123   synthetic calculations. After removing instrumental responses, the seismograms for VLFE
124   detection were resampled at one sample per second. We applied a bandpass filter in the frequency
125   range of 0.02–0.05 Hz (e.g., Ghosh et al., 2015; Ito et al., 2009; Takemura et al., 2019), because
126   this frequency band is less affected by microseismic noises (e.g., Hasselmann, 1963; Kaneko et al.,
127   2018). We verified that the large amplitude surface waves are generally matched well between
128   observed and synthetic waveforms in a higher frequency range (Figure S1; 0.02-0.06 Hz).

129   2.1.2. Matched-filter technique

130   The detection procedure used for VLFEs is similar to that used in our previous study (Baba
131   et al., 2020a). The horizontal-component seismograms of many stations were noisy; therefore, it
132   is difficult to use horizontal-component seismograms for the location of VLFEs (Figure S2). Thus,
133   we used only the vertical-component seismograms for the VLFE analysis although it is usual to
134   analyze VLFEs by using three-component seismograms. We placed 175 virtual source grids on
135   the Cocos Plate boundary at a uniform interval of 0.1° (Figure 2a) and computed synthetic
136   waveforms from these source grids to the stations in Costa Rica using an open-source seismic
137   wave propagation code (OpenSWPC; Maeda et al., 2017). We used a three-dimensional velocity
138   structure model constructed by combining CRUST 1.0 (Laske et al., 2013), Slab2 (Hayes et al.,
139   2018), and ETOPO1 (Amante & Eakins, 2009), setting the minimum *S*-wave velocity in the solid
140   columns to 1.0 km/s. We adopted the values of a mean oceanic slab structure (Christensen &
141   Salisbury, 1975) for the physical parameters of the subducting slab (Table S1). For the physical
142   parameters of the other layers except for the slab, we used the values of CRUST 1.0, and the default
143   parameter set of OpenSWPC. The cross-section of the structure model is shown in Figure S3. The
144   model covered the region enclosed by the red line (Figure 1b), which was discretized by a uniform
145   grid interval of 0.2 km. The assumed VLFE moment rate function was a Küpper wavelet with a
146   source duration of 15 s and an M_W of 4.0 (Figure 4 of Maeda et al., 2017). Since focal mechanisms
147   of VLFEs are shown to be consistent with shear slip on the plate boundaries in previous studies
148   (Cascadia: Ghosh et al., 2015; Nankai: Ito et al., 2009; Nakano et al., 2018; Sugioka et al., 2012;
149   Takemura et al., 2019), the focal mechanism at each source grid was assumed to be consistent with

150   the geometry of the plate boundary of Slab2 and the plate motion model, NUVEL-1A (DeMets et
151   al., 1994). The time window of each template was set to 150 s from the event origin time. Hereafter,
152   we simply refer to these synthetic waveforms as template waveforms. Examples of template
153   waveforms at updip and downdip source grids are shown in Figures 2b and 2c, respectively. The
154   signal first arrives at MANS and the variation of amplitudes is small for the updip source, whereas
155   signals first arriving at FINA exhibit amplitudes in or near the Nicoya Peninsula that are much
156   larger than in other areas for the downdip source.

157   We then calculated cross-correlation coefficients (CCs) between the filtered template
158   waveforms and observed seismograms every 1 s. We selected events with station-averaged
159   coefficients larger than a threshold defined as 9.5 times the median absolute deviation (MAD) of
160   the distributions. In order to decrease false detections by non-VLFE signals on the condition that
161   only the vertical-component seismograms can be used and the station coverage along the azimuth
162   direction is poor, we adopted a strict detection threshold compared to previous studies (e.g., 8 ×
163   MAD in Shelly et al., 2007, and Baba et al., 2018 and 9 × MAD in Baba et al., 2020a). The changes
164   of CCs when focal mechanisms or depths of assumed source models are different from the
165   geometry of the plate boundary are shown in Figure S4.

2.1.3. VLFE location and discarding false detections

167   Although a strict detection threshold was employed, there were false detections that are
168   caused by other signals, such as local or regional regular earthquakes or teleseismic events. To
169   exclude local or regional earthquakes, we compared the origin time of detected events with a
170   catalog of local and regional regular earthquakes constructed by El Observatorio Vulcanológico y
171   Sismológico de Costa Rica, Universidad Nacional (Catálogo de Temblores de Costa Rica, 2004-
172   2006; Protti, personal comm.). We discarded events whose epicentral distances were less than 150
173   km and origin times were within ±50 s from the local or regional earthquakes listed in this
174   earthquake catalog. To discard false detections by teleseismic events, we removed the events
175   detected between the *P*-wave arrivals and 600 s after *S*-wave arrivals of teleseismic events ($M_W \geq$
176   5) in the catalog of the United States Geological Survey. The event amplitudes and CCs are
177   positively correlated in general, but events with high amplitudes and low average CCs occasionally
178   appeared. These events can be considered to be false detections due to teleseismic events absent
179   in the catalogs. Therefore, we did not count events with average CCs below 0.56 and relative
180   amplitudes to templates higher than 0.4 (Baba et al., 2018; 2020a). If the amplitude relative to the
181   template with M_W of 4.0 was smaller than 0.05, we did not count the event because the signal was
182   too small to judge whether the event is truly existed or not.

183   For the remaining events, we calculated the variance reduction (VR) between the template
184   and observed waveforms. We estimated VRs using only the vertical-component seismograms of
185   relatively quiet stations in and around the Nicoya Peninsula (MANS, CABA, FINA, CRUP, and
186   PALM), because amplitude differences between updip and downdip events were large in these
187   stations:

$$VR = \left[1 - \frac{\sum_i \int \{f_i(t) - cg_i(t)\}^2 dt}{\sum_i \int \{f_i(t)\}^2 dt} \right] \times 100\% , \quad (1)$$

189   where $f_i(t)$ and $g_i(t)$ are the observed and template waveforms at the *i*-th station, respectively,
190   and *c* is the relative amplitude of the observed waveform to the template. We selected events whose
191   VRs were larger than 30%. A discarded example based on the VR is shown in Figure S5. This
192   threshold was set by trial and error based on visual identifications of VLFEs in the observed data.

193 After the above procedures, falsely detected events still remained because we only used the
194 vertical-component seismograms, and the array configuration was cross shaped. To discard the
195 remaining false detections, we estimated the normalized-and-stacked amplitude, azimuth, and
196 velocity of signal propagation by applying delay-and-sum beamforming (Section 3.1 of Rost &
197 Thomas, 2002; Walter et al., 2013) to vertical-component seismograms. After normalizing the
198 waveform of each station by its maximum amplitude in the 150 s time window, we searched for
199 the azimuth and velocity that maximized the stacked amplitude by performing a grid search for
200 the azimuth between 135–315º with 1º intervals and the velocity between 2–5 km/s with 0.1 km/s
201 intervals. We first used the along-strike stations in both Costa Rica and Nicaragua (brown inverted
202 triangles in Figure 1b) to discard teleseismic events. The amplitudes of Costa Rican VLFEs at the
203 Nicaraguan stations were generally very small compared with those in the Costa Rican stations
204 due to geometrical spreading, but amplitudes for teleseismic events are similar. Therefore, we
205 selected events whose stacked normalized amplitude normalized by the number of stations was
206 smaller than 0.6 because events with large stacked signals were suspected to be teleseismic
207 earthquakes (Figure S6). We then conducted another beamforming analysis for the remaining
208 events using the same stations as the matched-filter analysis, and selected events whose azimuth
209 was 200–230º. Finally, to avoid duplicate detection, only one event was counted every 60 s from
210 the remaining VLFE candidates. We only counted the event whose averaged CC was the highest
211 spatiotemporally.

2.1.4. Estimation of the moments of events

213 We estimated the source durations of detected VLFEs by comparing template waveforms
214 with source durations of 10–50 s with observed waveforms (e.g., Yabe et al., 2021). The M_W of
215 the templates was set to be 4.0. The source duration that resulted in the highest values of CC
216 between the observed and template waveforms was adopted.

217 We also calculated the amplitude of an event relative to the template waveforms using the
218 same method as Baba et al. (2020b). The relative amplitude was used to calculate the seismic
219 moment of each VLFE. The seismic moment rate of a VLFE was calculated by dividing its seismic
220 moment by its source duration. To evaluate the estimation error of moment rates of VLFEs, we
221 calculated moment rates by assuming the various source durations whose CCs between synthetic
222 and observed waveforms were more than 90% of the maximum CC. Although there are errors in
223 the order of 0.2, we verified that the order of moment rates did not change (Figure S7).

2.2. Results

225 We detected 68 VLFEs during the analysis period. Example traces of a VLFE located at
226 85.8°W and 9.4°N are shown in Figure3. The signal of this VLFE first arrives at MANS and
227 propagates to inland stations (top panel of Figure 3). This feature was successfully modeled for
228 the updip templates (Fig. 2b). There is a tremor signal in the frequency range of 2–8 Hz in the
229 same time window (middle and bottom panels of Figure 3). The cumulative number of VLFEs
230 showed significant increases in September 2004 and August 2005 (Figure 4a). In August 2005, an
231 SSE was reported by Jiang et al. (2012); therefore, SSE and VLFE activities were temporally
232 correlated. The M_W and source duration of VLFEs in Costa Rica were mainly distributed in 3.4–
233 4.2 and 10–30 s, respectively (Figures 5a, b).

234 Most of the detected VLFEs (62 events) are distributed where the plate boundary is at a
235 depth range of 6–10 km below the sea level, near the trench axis off the Nicoya Peninsula (Figure
236 4b), at the updip of the seismogenic zone. The distribution of these VLFEs is consistent with the

237 VLFEs in 2008 suggested by Walter et al. (2013). For the verifications of current results based on
238 only vertical components, we selected several events with relatively high signal-to-noise (SN)
239 ratios in horizontal components and located them using three-components seismograms. The
240 resultant high CC areas overlap and the epicenters were also located near the trench axis, although
241 there are differences of 0.1–0.2º (Figure S2). The area also overlaps with the shallower part of the
242 large slip area of the 2007 SSE (Jiang et al., 2017) or summed SSE slip in 2007–2012 (Dixon et
243 al., 2014). Although the slip distribution of the 2005 SSE was not estimated in previous studies,
244 our results suggest that the 2005 SSE can also have a large slip area near the trench axis, similar
245 to the 2007 SSE. The distribution of VLFEs lies within the gap between large slip areas of thrust-
246 type large interplate earthquakes with an M_W of 7–8 around the Nicoya Peninsula and the 1992
247 tsunami earthquake with an M_W of 7.6. The distribution of VLFEs also separated from the afterslip
248 area of the 2012 M_W 7.6 earthquake (Malservisi et al., 2015).

249   The distribution of the CC shows the resolution of the location of VLFEs. By the
250 distribution of CC, it is confirmed that most of the VLFEs were located near the trench axis. CCs
251 for more than half of the events exceeded the threshold only for updip templates (Figure 6a). For
252 several events, CCs exceeded the threshold both updip and downdip of the seismogenic zone with
253 a larger CC in the updip region. The area where CCs are more than 90% of the maximum CC is
254 concentrated only in the updip area (Figure 6b). On the other hand, 6 VLFEs were located at a
255 depth of ~40 km at the downdip of large earthquakes (Figure 4b). Although focal mechanisms may
256 not be thrust-type and the areas where CCs are larger than the threshold are widely distributed, we
257 verified that regular earthquakes listed in the earthquake catalog by El Observatorio Vulcanológico
258 y Sismológico de Costa Rica in the updip and downdip areas are located in the updip and downdip
259 areas respectively by this method (Figure S8). However, we cannot exclude the possibility that
260 such VLFEs occur in the updip region in real because, in such cases, bimodal CC distributions
261 tend to appear both in the updip and downdip (Figure 6c). Of course, there is a possibility that such
262 VLFEs really occur in the downdip region because the locations of such VLFEs were near the
263 locations of previously reported LFEs (Brown et al. 2009) and tremors (Outerbridge et al. 2010).
264 In this study, the SN ratios of VLFEs detected in the downdip region were very low; hence, it is
265 difficult to judge whether such VLFEs occur in downdip or updip, because it is hard to judge which
266 station the signal of the VLFE arrival first due to the similar arrival times at updip stations. The
267 reason for the small number and the low SN ratio of downdip events may be that slow earthquakes
268 in the downdip region were inactive during 1.5 years of the temporary array. To investigate
269 whether deep VLFEs really exist, an analysis with a longer dataset is needed in future work.

3. Estimations of seismic energy rates for tremors accompanied by VLFEs

3.1. Data and method

272   Tremor signals were also found in the frequency range of 2–8 Hz within the time windows
273 of detected VLFEs (middle panel of Figure 3; Figure S9). It is difficult to locate tremors in the
274 offshore region by using an onshore network because sources of tremors are distant from the
275 network and signals of tremors attenuate strongly compared to VLFE (0.02–0.05 Hz) signals.
276 Based on the spatiotemporal correlation between VLFEs and tremors reported in other regions
277 (e.g., Ghosh et al., 2015; Maeda & Obara, 2009; Tamaribuchi et al., 2019) and the interpretation
278 that VLFEs and tremors are components of broadband slow earthquake phenomena (Gomberg et
279 al., 2016; Hawthorne & Bartlow, 2018; Ide & Maury, 2018), we estimated the energy rate functions
280 of tremors accompanied by VLFEs by assuming that a tremor occurs at the same location as the
281 VLFE, i.e., the VLFE source grid with the highest CC as written in Section 2.1.3 (e.g., Yabe et al.,

282   2021). We simulated the waveforms at the location of a VLFE using the same model which is
283   described in Section 2.1.2 but discretized by a finer grid interval (0.04 km). The simulated
284   envelope shapes are different from observed ones due to a simple pulse source time function
285   (details in the caption of Figure S10), but the arrival times of maximum *S*-wave amplitudes in the
286   frequency range of 2–8 Hz are consistent with observed tremor waveforms (Figure S10). The
287   interval of source grids for the VLFE detection was set as 0.1º, therefore, we supposed that a VLFE
288   and the corresponding tremor occurred at the same location in the order of 10 km.

289   We also used waveforms of the TUCAN network similarly to the VLFE detection. After
290   applying a bandpass filter of 2–8 Hz, the envelope waveforms were calculated by taking the root-
291   mean-square of sums of three-component squared seismograms and a smoothing time window of
292   3 s (bottom panel of Figure 3). The envelope waveforms were resampled at one sample per second.

3.1.1. Quality factor of the apparent *S*-wave attenuation

294   To estimate the energy rate functions of tremors accurately, we estimated the quality factor
295   of the apparent *S*-wave attenuation ($Q_{app.}$), based on the coda-normalization method (e.g., Aki,
296   1980; Yoshimoto et al., 1993). First, we selected some isolated regular earthquakes (Figure S11).
297   To eliminate the effect of differences in source size and site amplification, observed maximum *S*-
298   wave amplitudes were normalized by averaged coda amplitudes within a lapse time of 80-90 s.
299   The coda-normalized maximum *S*-wave amplitude of the *i*-th earthquake at the *j*-th station (A_{ij})
300   and the distance between the hypocenter of the *i*-th earthquake and *j*-th station (L_{ij}) have the
301   following relationship (Takemura et al., 2017):

$$\ln\left(L_{ij}A_{ij}\right) = -\frac{\pi f_c Q_{app.}^{-1}}{V_s} L_{ij} + C' , \quad (2)$$

303   where V_s is the *S*-wave velocity (assuming 3.5 km/s in this study; Maeda & Obara, 2009; Yabe et
304   al., 2019; 2021), f_c is the central frequency (assuming 5 Hz in this study), and *C'* is a constant. By
305   solving Equation (2) by the least-squares method, we estimated $Q_{app.}^{-1}$ as $10^{-2.42}$ (Figure 7a).

3.1.2. Site amplification factor

307   We estimated the site amplification factor at 2–8 Hz using relative coda amplitudes (e.g.,
308   Maeda and Obara, 2009). Coda amplitudes at a certain time window generally depend on the
309   source size and site amplification (e.g., Chapters 2 and 3 of Sato et al., 2012). Therefore, the ratio
310   of the coda wave amplitude at a station to that at a reference station for the same event depends
311   only on the site amplification factor relative to a reference station.

312   We calculated the ratios of the coda amplitudes for each station to those of MANS
313   (reference station) for each regular earthquake used in Section 3.1. The time window for evaluating
314   relative coda amplitudes is the same as that in coda-normalization in Section 3.1. Then we
315   calculated the average of the coda amplitude ratios of all earthquakes for each station. The
316   estimated relative site amplification factors at each station used in the estimations of the energy
317   rate functions of tremors are shown in Figure 7b. We compared coda amplitudes of regular
318   earthquakes at MANS with those at the JTS, a permanent station of the Global Seismograph
319   Network by Incorporated Research Institutions for Seismology and International Deployment of
320   Accelerometers (Scripps Institution of Oceanography, 1986). The average ratio of coda amplitudes
321   at MANS to those at JTS is 1.14, suggesting that the condition of MANS site is very similar to that
322   of the JTS.

3.1.3. Seismic energy rate of tremors

324   By using apparent attenuation ($Q_{app.}^{-1}$) and site amplification in the previous subsections,
325 we estimated the energy rate functions of tremors. The source energy rate function of a tremor
326 ($E_j(t)$) using the amplitude of the *j*-th station is calculated by the following formula (Maeda &
327 Obara, 2009):

$$E_j(t) = 2\pi V_S r_j^2 \rho A_j'^2 (t + t_j) \exp\left(2\pi f_c Q_{app.}^{-1} t_j\right), \quad (3)$$

329 where $A'_j(t)$ is the site-corrected amplitude of the envelope waveform of the *j*-th station, r_j is the
330 hypocentral distance from the accompanying VLFE, t_j is the travel time from the VLFE source,
331 and ρ is the density (assuming 2,700 kg/m³). For calculating $E_j(t)$, we used a 180 s time window
332 that started 60 s before the origin time of VLFEs. We calculated the CCs of all station pairs in
333 Figure 7b. The range of CCs of each pair is 0.5–0.85 for the event of Figure 3 (Figure S12). To
334 estimate the source energy rate function of the tremor, we only used stations whose CCs with at
335 least one other station exceeded 0.6.

336   The seismic energy rate W_j using the amplitude of the *j*-th station is given by the integration
337 of the source energy rate function $E_j(t)$ in time:

$$W_j = \frac{1}{t_2 - t_1} \int_{t_1}^{t_2} E_j(t) dt, \quad (4)$$

339 where t_1 and t_2 are the start and end of the integration range, respectively. The integration range
340 was defined as the period in which the values of $E_j(t)$ exceeded 20% of the maximum value of
341 $E_j(t)$ (Figure 8). The seismic energy rate of a tremor (W_0) was obtained by calculating the average
342 W_j of all stations. The error of W_0 was obtained by calculating the standard deviation of W_j.

3.2. Results

344   For 13 of 68 VLFEs, there were no station pairs whose CCs were larger than 0.6 when
345 estimating the energy rates of accompanying tremors, because such tremors may not be detected
346 by technical limitations or tremors and VLFEs may be distinct phenomena. We, therefore,
347 estimated energy rates of 55 tremors. The energy rates of tremors were mainly distributed in 10^3–
348 $10^{5.5}$ J/s (Figure 9). There is a positive correlation between the energy rates of tremors and the
349 moment rates of the corresponding VLFEs. We estimated the scaled energy by calculating the ratio
350 between the seismic energy rate of a tremor and the seismic moment rate of the corresponding
351 VLFE. The scaled energy of slow earthquakes off Costa Rica is mainly distributed in the range of
352 10^{-9}–10^{-8} (dotted lines in Figure 9).

4. Discussion

4.1. Shallow ETS off Costa Rica

355   As shown in Figure 3 and Figure S9, VLFEs and tremors often were temporally correlated.
356 The activation of VLFEs and tremors in August 2005 temporally correlates with the 2005 SSE
357 reported by Jiang et al. (2012). VLFEs and tremors occurred mainly in the updip area in August
358 2005; hence, the slip area of the 2005 SSE can be distributed in the updip area near the trench axis,
359 similar to the 2007 SSE. In areas where shallow VLFEs occurred, subseafloor hydrological
360 observatories recorded pore fluid pressure transients in 2000 (Brown et al., 2005), 2003–2004
361 (Solomon et al., 2009), and 2007–2013 (Davis et al., 2011; 2015). They interpreted that pore fluid
362 pressure transients were caused by SSEs. Spatial correspondence of pore fluid change in the
363 periods of previous studies and VLFE activity in 2005 near the trench off Costa Rica suggests the

364 occurrence of a shallow ETS, as with the Nankai subduction zone (Araki et al., 2017; Nakano et
365 al., 2018).

4.2. Potential inferences of the frictional property on the plate boundary

367   To discuss the heterogeneity of the potential frictional property on the plate boundary, we
368 compare the differences of potential stress drops and interplate coupling between the VLFE area
369 and the seismogenic zone in the Central American subduction zone. The variability in the stress
370 drop reflects the variability of earthquake sources, which presumably represents a heterogeneity
371 in conditions at the sources (Abercrombie, 2021). In this study, we showed that most of VLFEs
372 were located at a depth range of 6–10 km on the plate boundary, which is updip of the seismogenic
373 zone. The stress drop of VLFEs in the Nankai subduction zone was estimated to be 0.1–10 kPa
374 (Ito & Obara, 2006), therefore we expect that the potential stress drop of VLFEs in Costa Rica is
375 similar. This is much smaller than the stress drop of earthquakes in the tsunami earthquake rupture
376 area (1.2 MPa; Bilek et al., 2016). In addition, the interplate coupling was estimated to be weak at
377 a depth range of 6–10 km (Feng et al., 2012), and strong in the seismogenic zone at a deeper depth
378 than 10 km (Protti et al., 2014).

379   The spatial variation of potential stress drops and interplate coupling at the plate boundary
380 may result from the heterogeneous distribution of potential frictional properties on the plate
381 boundary in the Central American subduction zone. In addition, a low stress drop suggests a high
382 pore pressure generated by the existence of fluids (Yao & Yang, 2020). Therefore, the potential
383 frictional strength of the slow earthquake area at a depth range of 6–10 km may be quite weak
384 owing to the rich fluid compared to that in the regions with regular and tsunami earthquakes.

385   In Costa Rica, repeating earthquakes occurred around the large coseismic slip area of the
386 2012 M_W 7.6 earthquake on the Nicoya Peninsula (Chaves et al., 2020). In this study, VLFEs were
387 mainly located near the trench axis, which is spatially separated from the locations of repeating
388 earthquakes that occur near the Nicoya Peninsula. Such spatial separation of slow and repeating
389 earthquakes on the plate boundary is also found in the Nankai (e.g., Takemura et al., 2020) and the
390 Tohoku subduction zone (e.g., Nishikawa et al., 2019).

4.3. Comparison with other subduction zones

392   The M_W and source duration of VLFEs have a positive correlation (Figure 5c) like shallow
393 VLFEs in Nankai, Japan (Sugioka et al., 2012; Takemura et al., 2019). Ide et al. (2007) suggested
394 that the relationship between durations and magnitudes of slow earthquakes is explained by 1st
395 power scaling law, whereas Dal Zilio et al. (2020) and Michel et al. (2019) inferred that the
396 relationship between moments and durations of SSEs is cubic. Although the number of cases is
397 small, it seems that durations and magnitudes of SSEs in Costa Rica (Voss et al., 2017) can be
398 explained by both 1st order and cubic scaling laws (Figure 5c). Jolivet & Frank (2020) suggested
399 that the difference between two scaling laws was caused by the ability to detect the beginnings and
400 ends of events. The relationship between moments and durations between both VLFEs and SSEs
401 is closer to the 1st power scaling law than the cubic scaling law.

402   Our study revealed that shallow VLFEs and tremors occurred near the trench axis off Costa
403 Rica, in the updip of coseismic slip areas of thrust-type large earthquakes with an M_W of 7–8. In
404 the updip area, SSEs also occurred in 2007–2012 (Dixon et al., 2017; Jiang et al., 2012). The depth
405 range and the separate distribution between shallow slow earthquakes and large earthquakes off
406 Costa Rica are similar to shallow slow earthquakes in the Nankai subduction zone, where slow

407   earthquakes are spatially separated from high slip-deficit zones (e.g., Takemura et al., 2020). On
408   the other hand, before the 2011 Tohoku earthquake, shallow slow slip events propagated to the
409   initial rupture point of the great earthquake (Kato et al., 2012). Therefore, the characteristics of
410   distribution of slow and large earthquakes differ between Tohoku and Costa Rica.

411   There are other common features in shallow slow earthquakes between Costa Rica and
412   Nankai. Although the lower limit of M_W is large (~3.4) due to a strict threshold, the ranges of
413   magnitudes and source durations of shallow VLFEs off Costa Rica are similar to those of shallow
414   VLFEs in the Nankai subduction zones (e.g., Takemura et al., 2019). The recurrence intervals of
415   activation of slow earthquakes are one to several years in Costa Rica (Jiang et al., 2012), which is
416   similar to shallow slow earthquakes in the Nankai subduction zone, but different from the shorter
417   intervals of deep slow earthquakes in Nankai (e.g., Baba et al., 2020b). Although the tremor
418   analysis is limited due to the missing of small events by the strict threshold of VLFEs, the range
419   of energy rates of tremors was 10^3–$10^{5.5}$ J/s. The upper limit of the energy rate range of tremors is
420   similar to that observed for shallow tremors in Nankai (Yabe et al., 2019). The estimated scaled
421   energy of slow earthquakes off Costa Rica is also similar to that of shallow slow earthquakes in
422   the Nankai subduction zone (Yabe et al., 2019). The scaled energy is related to the rupture process
423   of seismic phenomena (Kanamori & Rivera, 2006); therefore, the frictional properties within the
424   shallow slow earthquake areas may be similar in both Costa Rica and Nankai. On the other hand,
425   the scaled energy range in both regions is 0.5–1 orders of magnitude larger than that of shallow
426   slow earthquakes in the Tohoku subduction zone (Yabe et al., 2021), and approximately 1 order
427   of magnitude larger than that of deep slow earthquakes in Nankai (Ide et al., 2008; Ide &Yabe,
428   2014; Ide, 2016; Ide & Maury, 2018; Maeda & Obara, 2009) (Figure 9). We note that scaled
429   energies of shallow slow earthquakes were estimated for individual events, whereas those of deep
430   slow earthquakes estimated by Ide &Yabe (2014), Ide (2016), and Ide & Maury (2018) were
431   estimated for stacked events.

432   The range of scaled energy and distribution of shallow slow earthquakes off Costa Rica are
433   more similar to those in shallow Nankai than shallow Tohoku. According to Syracuse et al. (2010),
434   the age and thermal parameters of Costa Rica are 15.8 Ma and 1,010 km, respectively, which are
435   closer to those of Nankai (20.0 Ma and 450 km, respectively) than Tohoku (115.2–130.5 Ma and
436   5,720–6,040 km, respectively). The thermal parameter, which is product of the incoming plate age,
437   the convergence rate, and the sine of the slab dip angle, is used to predict the slab surface
438   temperature at a given depth (e.g., Kirby et al., 1991; Syracuse et al., 2010). In addition, the
439   temperatures of shallower parts of plate interfaces of these subduction zones where shallow slow
440   earthquakes are not so different (Nankai: ~100 ºC in the depth range of 0–5 km from the seafloor;
441   Tohoku: 65–110 ºC in the depth range of 6–12 km; and Costa Rica: 12–60ºC in the depth range of
442   0–10 km; modeled temperature in Saffer & Wallace, 2015). On the other hand, the Central
443   American subduction zone is subduction of fast convergence rate (~8 cm/year; DeMets et al.,
444   1994), high dip angle, and erosional type (e.g., Bangs et al., 2016), which are more similar to
445   Tohoku than Nankai. Although the characteristics of slow earthquake activity can be related to
446   various factors, the thermal parameter and incoming plate age of Costa Rica is more similar to
447   Nankai than Tohoku. The temperature structure of the shallow plate interface is probably most
448   sensitive to incoming plate age (Maunder et al., 2019) and secondarily to thermal parameter
449   (Syracuse et al., 2010). Hence, similar temperature conditions on the interface may explain the
450   common features of shallow slow earthquakes off Costa Rica and in Nankai.

451   In previous studies, the large slip area of the SSE in 2007 was separated into deeper and
452   shallower parts (Jiang et al., 2017), and deep LFEs and tremors were detected downdip of the
453   seismogenic zone (Brown et al., 2009; Outerbridge et al., 2010). And, several VLFEs were located
454   in the downdip area, in the similar area reported in previous studies of tremors and LFEs. If these
455   deep VLFEs, LFEs and tremors occur in the downdip area, slow earthquakes might occur at
456   separate depths along both shallower and deeper extensions of rupture zones of large earthquakes
457   (Figure 10). This characteristic might also be the same as that of the Nankai subduction zone
458   (Obara & Kato, 2016). This suggests that the tectonic property may be similar in the wide depth
459   range in Costa Rica and Nankai. On the other hand, slow earthquakes are distributed only in the
460   deeper part in the Cascadia subduction zone and only in the shallower part in the Tohoku
461   subduction zone. The variation of the distribution of slow earthquakes may be attributed to the
462   difference in tectonics or detection capability. The elucidation of the reason for the difference in
463   the distribution in slow earthquakes is future work.

464   **5. Conclusions**

465   Based on the grid-search matched-filter technique using synthetic templates in the regional
466   3D model, we detected and located VLFEs around the Nicoya Peninsula. Many VLFEs occurred
467   in September 2004 and August 2005, and more than 90% of the VLFEs were located near the
468   trench axis, where the plate boundary is at a depth range of 6–10 km, updip of the seismogenic
469   zone, whereas several VLFEs were located in the downdip area at a depth of ~40 km. In this area,
470   the occurrence of shallow SSEs is suggested by VLFE episodes. The region with VLFE activity
471   overlaps with the shallower part of the large slip area of the 2007 SSE; therefore, the occurrences
472   of shallow SSEs are suggested in September 2004 and August 2005 to occur in the same area as
473   the shallower part of the 2007 SSE. The distribution of VLFEs lies in the gap surrounding
474   coseismic slip areas of tsunami and large regular earthquakes. This separation reflects the spatial
475   distribution of the frictional strength of the plate boundary in the Central American subduction
476   zone. By using high-frequency seismogram envelopes, we also estimated the energy rates of
477   tremors accompanying VLFEs. The ranges of magnitude and source duration of VLFEs, energy
478   rate of tremors, and scaled energy off Costa Rica are similar to those in shallow slow earthquakes
479   in the Nankai subduction zone.

480   **Data Availability**

481   We used seismograms of the TUCAN network (Abers & Fischer, 2003;
482   https://doi.org/10.7914/SN/YO_2003) and Global Seismograph Network (Scripps Institution of
483   Oceanography, 1986; https://doi.org/10.7914/SN/II). We used the earthquake catalog of the U.S.
484   Geological Survey (https://earthquake.usgs.gov/earthquakes/search/). We used OpenSWPC code
485   Version 5.0.2 (Maeda et al., 2017; https://doi.org/10.5281/zenodo.3712650) for the numerical
486   simulations. Numerical simulations were conducted using the Fujitsu PRIMERGY
487   CX600M1/CX1640M1 (Oakforest-PACS) at the Information Technology Center, the University
488   of Tokyo. We used generic mapping tools (Wessel et al., 2013) and Seismic Analysis Code
489   (Helfrich et al., 2013) to prepare the figures and process seismograms, respectively. The VLFE
490   and tremor catalog constructed by this study is provided in an open access repository, zenodo (doi:
491   10.5281/zenodo.4435232).

501   **References**

502   Abercrombie, R. E. (2021). Resolution and uncertainties in estimates of earthquake stress drop
503   and energy release. *Philosophical Transactions of the Royal Society A*, 379: 20200131.
504   http://doi.org/10.1098/rsta.2020.0131
505   Abers, G. A., & Fischer, K. M. (2003). Tomography Under Costa Rica and Nicaragua.
506   International Federation of Digital Seismograph Networks.
507   https://doi.org/10.7914/SN/YO_2003
508   Aki, K. (1980). Attenuation of shear-waves in the lithosphere for frequencies from 0.05 to 25 Hz.
509   *Physics of the Earth and Planetary Interiors*, *21*(1), 50–60. https://doi.org/10.1016/0031-
510   9201(80)90019-9
511   Amante, C., & Eakins, B.W. (2009). ETOPO1 1 Arc-Minute Global Relief Model: Procedures,
512   Data Sources and Analysis. NOAA Technical Memorandum NESDIS NGDC-24.
513   https://doi.org/10.7289/V5C8276M
514   Araki, E., Saffer, D. M., Kopf, A. J., Wallace, L. M., Kimura, T., Machida, Y., Ide, S., Davis, E.,
515   & IODP Expedition 365 shipboard scientists (2017). Recurring and triggered slow-slip
516   events near the trench at the Nankai Trough subduction megathrust. *Science*, *356*(6343),
517   1157–1160. https://doi.org/10.1126/science.aan3120
518   Baba, S., Takeo, A., Obara, K., Kato, A., Maeda, T., & Matsuzawa, T. (2018). Temporal
519   Activity Modulation of Deep Very Low Frequency Earthquakes in Shikoku, Southwest
520   Japan. *Geophysical Research Letters*, *45*(2), 733–738.
521   https://doi.org/10.1002/2017GL076122
522   Baba, S., Takeo, A., Obara, K., Matsuzawa, T., & Maeda, T. (2020a). Comprehensive Detection
523   of Very Low Frequency Earthquakes Off the Hokkaido and Tohoku Pacific Coasts,
524   Northeastern Japan. *Journal of Geophysical Research: Solid Earth*, *125*(1), 1–13.
525   https://doi.org/10.1029/2019JB017988
526   Baba, S., Takemura, S., Obara, K., & Noda, A. (2020b). Slow Earthquakes Illuminating
527   Interplate Coupling Heterogeneities in Subduction Zones. *Geophysical Research Letters*,
528   *47*(14), 4–5. https://doi.org/10.1029/2020GL088089
529   Bangs, N. L., McIntosh, K. D., Silver, E. A., Kluesner, J. W., & Ranero, C. R. (2016). A recent
530   phase of accretion along the southern Costa Rican subduction zone. *Earth and Planetary
531   Science Letters*, *443*, 204–215. https://doi.org/10.1016/j.epsl.2016.03.008
532   Bilek, S. L., Rotman, H. M. M., & Phillips, W. S. (2016). Low stress drop earthquakes in the
533   rupture zone of the 1992 Nicaragua tsunami earthquake. *Geophysical Research Letters*,
534   *43*(19), 10,180-10,188. https://doi.org/10.1002/2016GL070409

13

Brown, J. R., Beroza, G. C., Ide, S., Ohta, K., Shelly, D. R., Schwartz, S. Y., et al. (2009). Deep low-frequency earthquakes in tremor localize to the plate interface in multiple subduction zones. *Geophysical Research Letters*, *36*(19), 1–5. https://doi.org/10.1029/2009GL040027

Brown, K. M., Tryon, M. D., DeShon, H. R., Dorman, L. R. M., & Schwartz, S. Y. (2005). Correlated transient fluid pulsing and seismic tremor in the Costa Rica subduction zone. *Earth and Planetary Science Letters*, *238*(1–2), 189–203. https://doi.org/10.1016/j.epsl.2005.06.055

Chaves, E. J., Schwartz, S. Y., & Abercrombie, R. E. (2020). Repeating earthquakes record fault weakening and healing in areas of megathrust postseismic slip. *Science Advances, 6*(32), eaaz9317. https://doi.org/10.1126/sciadv.aaz9317

Christensen, N. I., & Salisbury, M. H. (1975). Structure and constitution of the lower oceanic crust. *Reviews of Geophysics*, *13*(1), 57–86. https://doi.org/10.1029/RG013i001p00057

Dal Zilio, L., Lapusta, N., & Avouac, J.-P. (2020). Unraveling scaling properties of slow-slip events. Geophysical Research Letters, 47, e2020GL087477. https://doi.org/10.1029/2020GL087477

Davis, E., Heesemann, M., & Wang, K. (2011). Evidence for episodic aseismic slip across the subduction seismogenic zone off Costa Rica: CORK borehole pressure observations at the subduction prism toe. *Earth and Planetary Science Letters*, *306*(3–4), 299–305. https://doi.org/10.1016/j.epsl.2011.04.017

Davis, E. E., Villinger, H., & Sun, T. (2015). Slow and delayed deformation and uplift of the outermost subduction prism following ETS and seismogenic slip events beneath Nicoya Peninsula, Costa Rica. *Earth and Planetary Science Letters*, *410*, 117–127. https://doi.org/10.1016/j.epsl.2014.11.015

DeMets, C., Gordon, R. G., Argus, D. F., & Stein, S. (1994). Effect of recent revisions to the geomagnetic reversal time scale on estimates of current plate motions. *Geophysical Research Letters*, *21*(20), 2191–2194. https://doi.org/10.1029/94GL02118

Dixon, T. H., Jiang, Y., Malservisi, R., McCaffrey, R., Voss, N., Protti, M., & Gonzalez, V. (2014). Earthquake and tsunami forecasts: Relation of slow slip events to subsequent earthquake rupture. *Proceedings of the National Academy of Sciences of the United States of America*, *111*(48), 17039–17044. https://doi.org/10.1073/pnas.1412299111

Dragert, H., Wang, K., James, T. S. (2001). A Silent Slip Event on the Deeper Cascadia Subduction Interface. *Science*, *292*(5521), 1525–1528. https://doi.org/10.1126/science.1060152

Feng, L., Newman, A. V., Protti, M., Gonzlez, V., Jiang, Y., & Dixon, T. H. (2012). Active deformation near the Nicoya Peninsula, northwestern Costa Rica, between 1996 and 2010: Interseismic megathrust coupling. *Journal of Geophysical Research: Solid Earth*, *117*(6), 1–23. https://doi.org/10.1029/2012JB009230

Ghosh, A., Huesca-Pérez, E., Brodsky, E., & Ito, Y. (2015). Very low frequency earthquakes in Cascadia migrate with tremor. *Geophysical Research Letters*, *42*(9), 3228–3232. https://doi.org/10.1002/2015GL063286

Gomberg, J., Wech, A., Creager, K., Obara, K., & Agnew, D. (2016). Reconsidering earthquake scaling. *Geophysical Research Letters*, *43*(12), 6243–6251. https://doi.org/10.1002/2016GL069967

Hawthorne, J. C., & Bartlow, N. M. (2018). Observing and Modeling the Spectrum of a Slow Slip Event. *Journal of Geophysical Research: Solid Earth*, *123*(5), 4243–4265. https://doi.org/10.1029/2017JB015124

581 Hasselmann, K. (1963). A statistical analysis of the generation of microseisms. *Reviews of*
582   *Geophysics*, 1, 177–209. https://doi.org/10.1029/RG001i002p00177
583 Hayes, G. P., Moore, G. L., Portner, D. E., Hearne, M., Flamme, H., Furtney, M., & Smoczyk,
584   G. M. (2018). Slab2, a Comprehensive Subduction Zone Geometry Model, *Science*,
585   61(October), 58–61. https://doi.org/10.1126/science.aat4723
586 Helffrich, G., Wookey, J., & Bastow, I. (2013). The Seismic Analysis Code. Cambridge:
587   Cambridge University Press. https://doi.org/10.1017/CBO9781139547260
588 Hutchison, A. A. (2020). Interepisodic Tremor and Slip Event Episodes of Quasi-
589   spatiotemporally Discrete Tremor and Very Low Frequency Earthquakes in Cascadia
590   Suggestive of a Connective Underlying, Heterogeneous Process. *Geophysical Research*
591   *Letters*, *47*(3), 1–7. https://doi.org/10.1029/2019GL086798
592 Hutchison, A. A., & Ghosh, A. (2016). Very low frequency earthquakes spatiotemporally
593   asynchronous with strong tremor during the 2014 episodic tremor and slip event in
594   Cascadia. *Geophysical Research Letters*, *43*(13), 6876–6882.
595   https://doi.org/10.1002/2016GL069750
596 Hutchison, A. A., & Ghosh, A. (2019). Repeating VLFEs During ETS Events in Cascadia Track
597   Slow Slip and Continue Throughout Inter-ETS Period. *Journal of Geophysical Research:*
598   *Solid Earth*, *124*(1), 554–565. https://doi.org/10.1029/2018JB016138
599 Ide, S. (2016). Characteristics of slow earthquakes in the very low frequency band: Application
600   to the Cascadia subduction zone. *Journal of Geophysical Research: Solid Earth*, *121*(8),
601   5942–5952. https://doi.org/10.1002/2016JB013085
602 Ide, S., & Maury, J. (2018). Seismic Moment, Seismic Energy, and Source Duration of Slow
603   Earthquakes: Application of Brownian slow earthquake model to three major subduction
604   zones. *Geophysical Research Letters*, *45*(7), 3059–3067.
605   https://doi.org/10.1002/2018GL077461
606 Ide, S., & Yabe, S. (2014). Universality of slow earthquakes in the very low frequency band.
607   *Geophysical Research Letters*, *41*(8), 2786–2793. https://doi.org/10.1002/2014GL059712
608 Ide, S., Beroza, G. C., Shelly, D. R., & Uchide, T. (2007). A scaling law for slow earthquakes.
609   *Nature*, *447*(7140), 76–79. https://doi.org/10.1038/nature05780
610 Ide, S., Imanishi, K., Yoshida, Y., Beroza, G. C., & Shelly, D. R. (2008). Bridging the gap
611   between seismically and geodetically detected slow earthquakes. *Geophysical Research*
612   *Letters*, *35*(10), 2–7. https://doi.org/10.1029/2008GL034014
613 Ito, Y., Obara, K., Shiomi, K., Sekine, S., & Hirose, H. (2007). Slow Earthquakes Coincident
614   with Episodic Tremors and Slow Slip Events. *Science*, *315*(5811), 503–506.
615   https://doi.org/10.1126/science.1134454
616 Ito, Y., & Obara, K. (2006). Very low frequency earthquakes within accretionary prisms are very
617   low stress-drop earthquakes. *Geophysical Research Letters*, *33*(9), 1–4.
618   https://doi.org/10.1029/2006GL025883
619 Ito, Y., Obara, K., Matsuzawa, T., & Maeda, T. (2009). Very low frequency earthquakes related
620   to small asperities on the plate boundary interface at the locked to aseismic transition.
621   *Journal of Geophysical Research: Solid Earth*, *114*(11), 1–16.
622   https://doi.org/10.1029/2008JB006036
623 Ito, Y., Hino, R., Kido, M., Fujimoto, H., Osada, Y., Inazu, D., et al. (2013). Episodic slow slip
624   events in the Japan subduction zone before the 2011 Tohoku-Oki earthquake.
625   *Tectonophysics*, *600*, 14–26. https://doi.org/10.1016/j.tecto.2012.08.022

626 Jiang, Y., Wdowinski, S., Dixon, T. H., Hackl, M., Protti, M., & Gonzalez, V. (2012). Slow slip
627   events in Costa Rica detected by continuous GPS observations, 2002-2011. *Geochemistry,*
628   *Geophysics, Geosystems*, *13*(1), 1–18. https://doi.org/10.1029/2012GC004058
629 Jiang, Y., Liu, Z., Davis, E. E., Schwartz, S. Y., Dixon, T. H., Voss, N., et al. (2017). Strain
630   release at the trench during shallow slow slip: The example of Nicoya Peninsula, Costa
631   Rica. *Geophysical Research Letters*, *44*(10), 4846–4854.
632   https://doi.org/10.1002/2017GL072803
633 Jolivet, R & Frank, W. B. (2020). The transient and intermittent nature of slow slip. AGU
634   Advances, 1, e2019AV000126. https://doi.org/10. 1029/2019AV000126
635 Kanamori, H., & Rivera, L. (2006). Energy partitioning during an earthquake. *Geophysical*
636   *Monograph Series*, *170*, 3–13. https://doi.org/10.1029/170GM03
637 Kaneko, L., Ide, S., & Nakano, M. (2018). Slow Earthquakes in the Microseism Frequency Band
638   (0.1–1.0 Hz) off Kii Peninsula, Japan. *Geophysical Research Letters*, *45*(6), 2618–2624.
639   https://doi.org/10.1002/2017GL076773
640 Kato, A., & Nakagawa, S. (2014). Geophysical Research Letters. *Geophysical Research Letters*,
641   (April), 6413–6419. https://doi.org/10.1002/2014GL061184.Received
642 Kato, A., Obara, K., Igarashi, T., Tsuruoka, H., Nakagawa, S., & Hirata, N. (2012). Propagation
643   of Slow Slip Leading Up to the 2011 Mw 9.0 Tohoku-Oki Earthquake. *Science*, *335*(6069),
644   705–708. https://doi.org/10.1126/science.1215141
645 Kirby, S. T., Durham, W. B., & Stern, L. A. (1991). Mantle Phase Changes and Deep-
646   Earthquake Faulting in Subducting Lithosphere. *Science*, 252(5003), 216-225.
647   https://doi.org/10.1126/science.252.5003.216
648 Laske, G., Masters., G., Ma, Z., & Pasyanos, M. (2013). Update on CRUST1.0 - A 1-degree
649   Global Model of Earth's Crust, Paper presented at EGU General Assembly, European
650   Geoscience Union, Vienna
651 Maeda, T., & Obara, K. (2009). Spatiotemporal distribution of seismic energy radiation from
652   low-frequency tremor in western Shikoku, Japan. *Journal of Geophysical Research: Solid*
653   *Earth*, *114*(10). https://doi.org/10.1029/2008JB006043
654 Maeda, T., Takemura, S., & Furumura, T. (2017). OpenSWPC: An open-source integrated
655   parallel simulation code for modeling seismic wave propagation in 3D heterogeneous
656   viscoelastic media 4. Seismology. *Earth, Planets and Space*, *69*(1).
657   https://doi.org/10.1186/s40623-017-0687-2
658 Malservisi, R., Schwartz, S.Y., Voss, N., Protti, M., Gonzalez, V., Dixon, T.H., Jian, Y.,
659   Newman, A.V., Walter, J.I., & Voyenko, D. (2015). Multiscale postseismic behavior on a
660   megathrust: The 2012 Nicoya earthquake, Costa Rica. *Geochemistry, Geophysics,*
661   *Geosystems*, 16, 1848–1864. https://doi.org/10.1002/2015GC005794.
662 Maunder, B., van Hunen, J., Bouilhol, P., & Magni, V. (2019). Modeling Slab Temperature: A
663   Reevaluation of the Thermal Parameter. *Geochemistry, Geophysics, Geosystems*, *20*(2),
664   673–687. https://doi.org/10.1029/2018GC007641
665 Michel, S., Gualandi, A., & Avouac, J. (2019). Similar scaling laws for earthquakes and
666   Cascadia slow-slip events. Nature, 574, 522-526. https://doi.org/10.1038/s41586-019-1673-
667   6
668 Nadeau, R. M., & Dolenc, D. (2005). Nonvolcanic tremors deep beneath the San Andreas Fault.
669   *Science*, *307*(5708), 389. https://doi.org/10.1126/science.1107142
670 Nakano, M., Hori, T., Araki, E., Kodaira, S., & Ide, S. (2018). Shallow very-low-frequency
671   earthquakes accompany slow slip events in the Nankai subduction zone /704/2151/210

672   /704/2151/508 article. *Nature Communications*, *9*(1). https://doi.org/10.1038/s41467-018-
673   03431-5
674 Nishikawa, T., Matsuzawa, T., Ohta, K., Uchida, N., Nishimura, T., & Ide, S. (2019). The slow
675   earthquake spectrum in the Japan Trench illuminated by the S-net seafloor observatories.
676   *Science (New York, N.Y.)*, *365*(6455), 808–813. https://doi.org/10.1126/science.aax5618
677 Obara, K. (2002). Nonvolcanic Deep Tremor Associated with Subduction in Southwest Japan.
678   *Science*, *296*(5573), 1679–1681. https://doi.org/10.1126/science.1070378
679 Obara, K. (2011). Characteristics and interactions between non-volcanic tremor and related slow
680   earthquakes in the Nankai subduction zone, southwest Japan. *Journal of Geodynamics*,
681   *52*(3–4), 229–248. https://doi.org/10.1016/j.jog.2011.04.002
682 Obara, K., & Ito, Y. (2005). Very low frequency earthquakes excited by the 2004 off Kii
683   peninsula earthquakes: A dynamic deformation process in the large accretionary prism.
684   *Earth, Planets and Space*, *57*(4), 321–326. https://doi.org/10.1186/BF03352570
685 Obara, K., & Kato, A. (2016). Connecting slow earthquakes to huge earthquakes. *Science (New*
686   *York, N.Y.)*, *353*(6296), 253–257. https://doi.org/10.1126/science.aaf1512
687 Outerbridge, K. C., Dixon, T. H., Schwartz, S. Y., Walter, J. I., Protti, M., Gonzalez, V., et al.
688   (2010). A tremor and slip event on the Cocos-Caribbean subduction zone as measured by a
689   global positioning system (GPS) and seismic network on the Nicoya Peninsula, Costa Rica.
690   *Journal of Geophysical Research: Solid Earth*, *115*(10), 1–17.
691   https://doi.org/10.1029/2009JB006845
692 Protti, M. (1995). The March 25, 1990 (Mw=7.0, ML=6.8), earthquake at the entrance of the
693   Nicoya Gulf, Costa Rica: its prior activity, foreshocks, aftershocks, and triggered seismicity.
694   *Journal of Geophysical Research*, *100*(B10), 345–358. https://doi.org/10.1029/94jb03099
695 Protti, M., González, V., Newman, A. V., Dixon, T. H., Schwartz, S. Y., Marshall, J. S., et al.
696   (2014). Nicoya earthquake rupture anticipated by geodetic measurement of the locked plate
697   interface. *Nature Geoscience*, *7*(2), 117–121. https://doi.org/10.1038/ngeo2038
698 Rogers, G., & Dragert, H. (2003). Episodic Tremor and Slip on the Cascadia Subduction Zone:
699   The Chatter of Silent Slip. *Science*, *300*(5627), 1942–1943.
700   https://doi.org/10.1126/science.1084783
701 Rost, S., & Thomas, C. (2002). Array seismology: Methods and applications. *Reviews of*
702   *Geophysics*, *40*(3), 2-1-2–27. https://doi.org/10.1029/2000RG000100
703 Ruiz, S., Aden-Antoniow, F., Baez, J. C., Otarola, C., Potin, B., del Campo, F., et al. (2017).
704   Nucleation Phase and Dynamic Inversion of the M w 6.9 Valparaíso 2017 Earthquake in
705   Central Chile. *Geophysical Research Letters*, *44*(20), 10,290-10,297.
706   https://doi.org/10.1002/2017GL075675
707 Saffer, D. M., & Wallace, L. M. (2015). The frictional, hydrologic, metamorphic and thermal
708   habitat of shallow slow earthquakes. *Nature Geoscience*, *8*(8), 594–600.
709   https://doi.org/10.1038/ngeo2490
710 Satake, K. (1994). Mechanism of the 1992 Nicaragua Tsunami Earthquake. *Geophysical*
711   *Research Letters*, *21*(23), 2519–2522. https://doi.org/10.1029/94GL02338
712 Sato, H., Fehler, M., & Maeda, T. (2012). Seismic Wave Propagation and Scattering in the
713   Heterogeneous Earth Structure, 2nd ed., New York, Springer-Verlag.
714 Scripps Institution of Oceanography. (1986). IRIS/IDA Seismic Network. International
715   Federation of Digital Seismograph Networks. https://doi.org/10.7914/SN/II

716 Shelly, D. R., Beroza, G. C., Ide, S., & Nakamula, S. (2006). Low-frequency earthquakes in
717   Shikoku, Japan, and their relationship to episodic tremor and slip. *Nature*, *442*(7099), 188–
718   191. https://doi.org/10.1038/nature04931
719 Shelly, D. R., Beroza, G. C., & Ide, S. (2007). Non-volcanic tremor and low-frequency
720   earthquake swarms. *Nature*, *446*(7133), 305–307. https://doi.org/10.1038/nature05666
721 Solomon, E. A., Kastner, M., Wheat, C. G., Jannasch, H., Robertson, G., Davis, E. E., & Morris,
722   J. D. (2009). Long-term hydrogeochemical records in the oceanic basement and forearc
723   prism at the Costa Rica subduction zone. *Earth and Planetary Science Letters*, *282*(1–4),
724   240–251. https://doi.org/10.1016/j.epsl.2009.03.022
725 Sugioka, H., Okamoto, T., Nakamura, T., Ishihara, Y., Ito, A., Obana, K., et al. (2012).
726   Tsunamigenic potential of the shallow subduction plate boundary inferred from slow
727   seismic slip. *Nature Geoscience*, *5*(6), 414–418. https://doi.org/10.1038/ngeo1466
728 Syracuse, E. M., van Keken, P. E., Abers, G. A., Suetsugu, D., Bina, C., Inoue, T., et al. (2010).
729   The global range of subduction zone thermal models. *Physics of the Earth and Planetary
730   Interiors*, *183*(1–2), 73–90. https://doi.org/10.1016/j.pepi.2010.02.004
731 Takemura, S., Kobayashi, M., & Yoshimoto, K. (2017). High-frequency seismic wave
732   propagation within the heterogeneous crust: Effects of seismic scattering and intrinsic
733   attenuation on ground motion modelling. *Geophysical Journal International*, *210*(3), 1806–
734   1822. https://doi.org/10.1093/gji/ggx269
735 Takemura, S., Matsuzawa, T., Noda, A., Tonegawa, T., Asano, Y., Kimura, T., & Shiomi, K.
736   (2019). Structural Characteristics of the Nankai Trough Shallow Plate Boundary Inferred
737   From Shallow Very Low Frequency Earthquakes. *Geophysical Research Letters*, *46*(8),
738   4192–4201. https://doi.org/10.1029/2019GL082448
739 Takemura, S., Okuwaki, R., Kubota, T., Shiomi, K., Kimura, T., & Noda, A. (2020). Centroid
740   moment tensor inversions of offshore earthquakes using a three-dimensional velocity
741   structure model: slip distributions on the plate boundary along the Nankai Trough.
742   *Geophysical Journal International*, *222*(2), 1109–1125. https://doi.org/10.1093/gji/ggaa238
743 Tamaribuchi, K., Kobayashi, A., Nishimiya, T., Hirose, F., & Annoura, S. (2019).
744   Characteristics of Shallow Low-Frequency Earthquakes off the Kii Peninsula, Japan, in
745   2004 Revealed by Ocean Bottom Seismometers. *Geophysical Research Letters*, *46*(23),
746   13737–13745. https://doi.org/10.1029/2019GL085158
747 Voss, N., Dixon, T. H., Liu, Z., Malservisi, R., Protti, M., & Schwartz, S. (2018). Do slow slip
748   events trigger large and great megathrust earthquakes? *Science Advances*, *4*(10), 1–6.
749   https://doi.org/10.1126/sciadv.aat8472
750 Voss, N. K., Malservisi, R., Dixon, T. H., & Protti, M. (2017). Slow slip events in the early part
751   of the earthquake cycle. *Journal of Geophysical Research: Solid Earth*, *122*(8), 6773–6786.
752   https://doi.org/10.1002/2016JB013741
753 Walter, J. I., Schwartz, S. Y., Protti, J. M., & Gonzalez, V. (2011). Persistent tremor within the
754   northern Costa Rica seismogenic zone. *Geophysical Research Letters*, *38*(1), 1–5.
755   https://doi.org/10.1029/2010GL045586
756 Walter, J. I., Schwartz, S. Y., Protti, M., & Gonzalez, V. (2013). The synchronous occurrence of
757   shallow tremor and very low frequency earthquakes offshore of the Nicoya Peninsula, Costa
758   Rica. *Geophysical Research Letters*, *40*(8), 1517–1522. https://doi.org/10.1002/grl.50213
759 Wang, L., & Barbot, S. (2020). Excitation of San Andreas tremors by thermal instabilities below
760   the seismogenic zone. *Science Advances*, *6*(36). https://doi.org/10.1126/sciadv.abb2057

761 Wessel, P., Smith, W. H. F., Scharroo, R., Luis, J., & Wobbe, F. (2013). Generic mapping tools:
762   Improved version released. *Eos*, *94*(45), 409–410. https://doi.org/10.1002/2013EO450001
763 Xie, S., Dixon, T. H., Malservisi, R., Jiang, Y., Protti, M., & Muller, C. (2020). Slow Slip and
764   Inter-transient Locking on the Nicoya Megathrust in the Late and Early Stages of an
765   Earthquake Cycle. *Journal of Geophysical Research: Solid Earth*, *125*(11), 1–22.
766   https://doi.org/10.1029/2020JB020503
767 Yabe, S., Tonegawa, T., & Nakano, M. (2019). Scaled Energy Estimation for Shallow Slow
768   Earthquakes. *Journal of Geophysical Research: Solid Earth*, *124*(2), 1507–1519.
769   https://doi.org/10.1029/2018JB016815
770 Yabe, S., Baba, S., Tonegawa, T., Nakano, M., & Takemura, S. (2021). Seismic energy radiation
771   and along-strike heterogeneities of shallow tectonic tremors at the Nankai Trough and Japan
772   Trench. *Tectonophysics*, 228714. https://doi.org/10.1016/j.tecto.2020.228714
773 Yao, S., & Yang, H. (2020). Rupture Dynamics of the 2012 Nicoya Mw 7.6 Earthquake:
774   Evidence for Low Strength on the Megathrust. *Geophysical Research Letters*, *47*(13), 1–11.
775   https://doi.org/10.1029/2020GL087508
776 Yokota, Y., & Ishikawa, T. (2020). Shallow slow slip events along the Nankai Trough detected
777   by GNSS-A. *Science Advances*, *6*(3), 1–12. https://doi.org/10.1126/sciadv.aay5786
778 Yoshimoto, K., Sato, H., & Ohtake, M. (1993). Frequency-Dependent Attenuation of P and S
779   Waves In the Kanto Area, Japan, Based On the Coda-Normalization Method. *Geophysical*
780   *Journal International*, *114*(1), 165–174. https://doi.org/10.1111/j.1365-
781   246X.1993.tb01476.x
782 Yue, H., Lay, T., Schwartz, S. Y., Rivera, L., Protti, M., Dixon, T. H., et al. (2013). The 5
783   September 2012 Nicoya, Costa Rica Mw 7.6 earthquake rupture process from joint
784   inversion of high-rate GPS, strong-motion, and teleseismic P wave data and its relationship
785   to adjacent plate boundary interface properties. *Journal of Geophysical Research: Solid*
786   *Earth*, *118*(10), 5453–5466. https://doi.org/10.1002/jgrb.50379
787
788
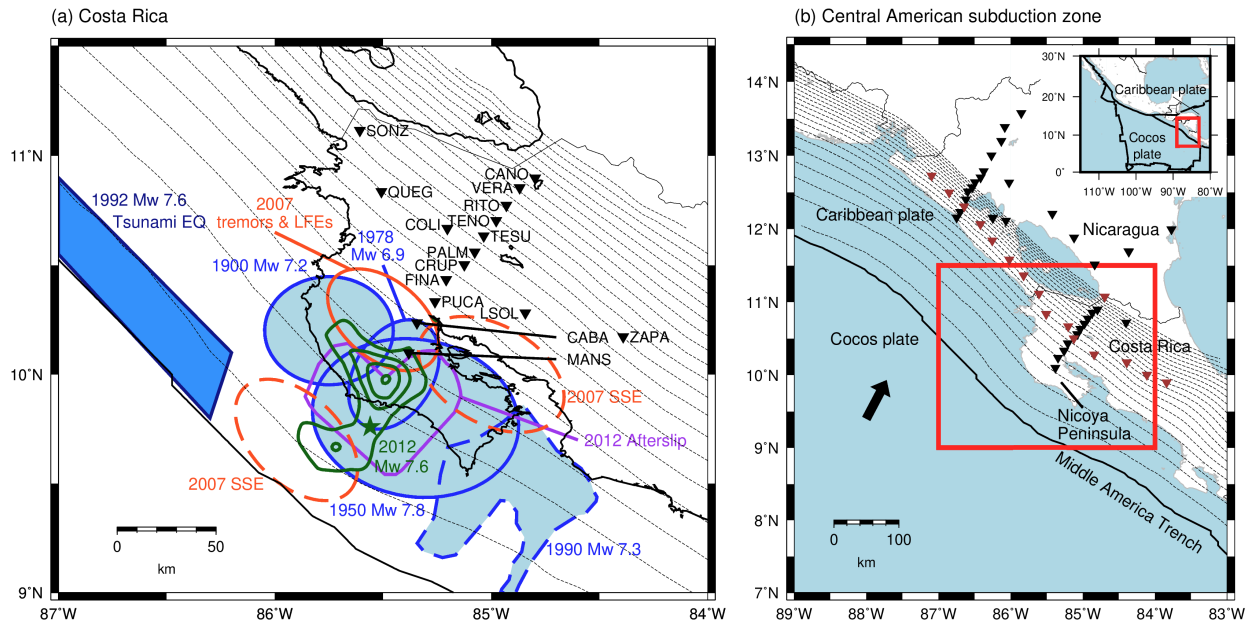
Figure 1. (a) Large regular and slow earthquake areas based on previous studies around the Nicoya Peninsula, in Costa Rica. Green contours show the coseismic slip distribution of the 2012 M_W 7.6 earthquake with a 1-m interval (Yue et al., 2013). Blue areas show the slip areas of large regular earthquakes (1990 M_W 7.3: Protti et al., 1995 (surrounded by dashed blue line); others: Yue et al., 2013 (surrounded by solid blue lines)). Dark blue area surrounded by solid dark blue line indicate the slip area of the 1992 tsunami earthquake (Satake, 1994). Orange ellipses with dashed lines show large slip areas of the 2007 SSE, which were separated in updip and downdip areas (Jiang et al., 2017). The orange ellipse with a solid line shows the distributions of LFEs (Brown et al., 2009) and tremors (Outerbridge et al., 2010). The purple polygon shows the area whose afterslip of the 2012 M_W 7.6 earthquake is more than 150 mm (Malvervisi et al., 2015). Black inverted triangles show the station locations of the TUCAN network used in VLFE detection (Section 2.2). Dashed contours indicate the isodepths of the top of the Cocos Plate with 10 km intervals (Slab2; Hayes et al., 2018). (b) Map of the Central American subduction zone. Solid line represents the Middle America Trench (Slab2; Hayes et al., 2018). Dashed contours are the same as (a). Black arrow indicates the convergence direction of the Cocos Plate, which subducts below the Caribbean plate from the Middle America Trench (NUVEL-1A; DeMets et al., 1994). Inverted triangles show the locations of stations of the TUCAN network. Brown triangles are stations which were used in beamforming (Section 2.3). The black lines in the inset show plate boundaries.
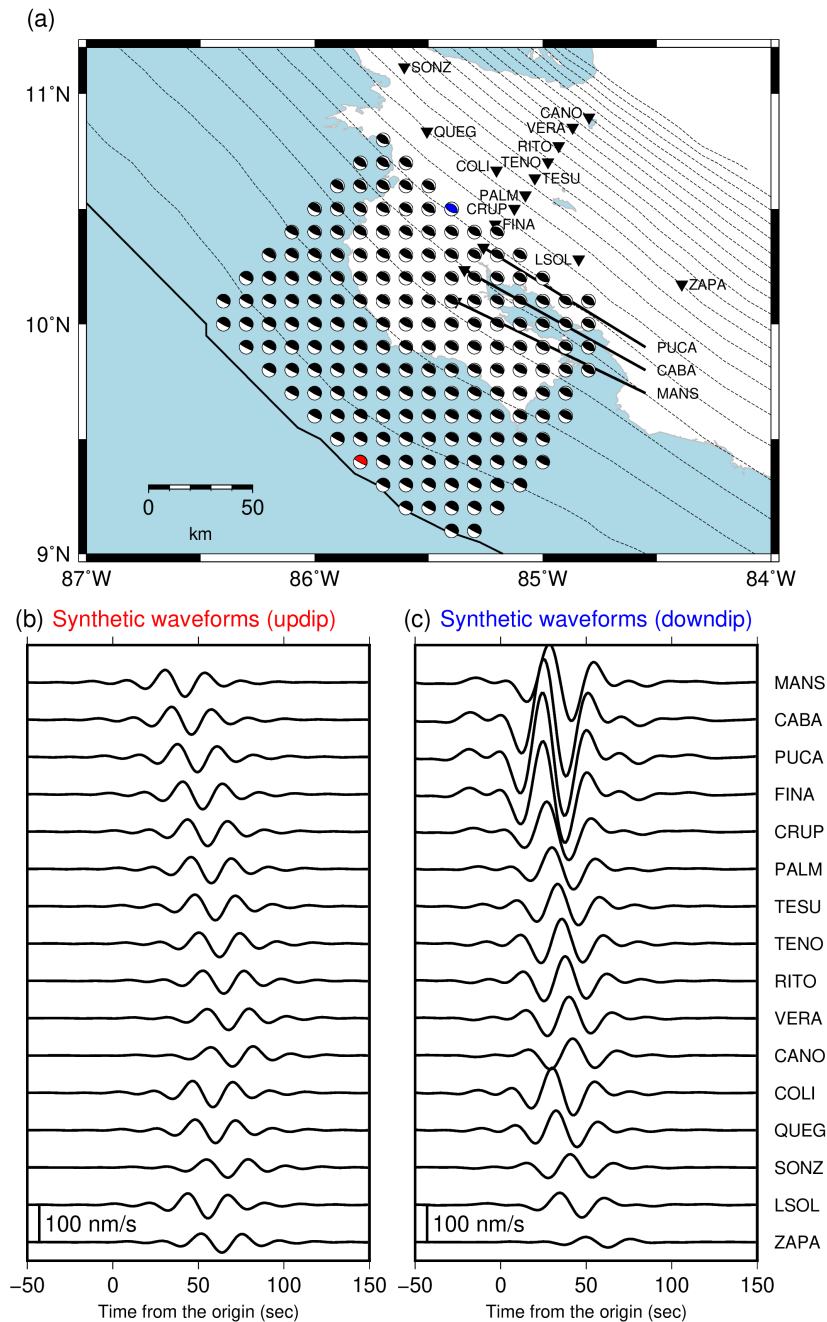
Figure 2. (a) Virtual source grids assumed in this study. Beach balls show the locations and focal mechanisms of the virtual sources. Inverted triangles and the black line are the same as in Figure 1. Dashed contours indicate the isodepths of the top of the Cocos Plate with 10 km intervals (Slab2; Hayes et al., 2018). Examples of waveforms of virtual sources with Mw 4 in the (b) updip and (c) downdip areas. Sources of Figures 1b and 1c are shown by the red and blue beachballs in Figure 2a, respectively. Amplitudes of the updip source are small due to the long distance between the source and stations, whereas amplitudes of the downdip source in the stations near the Nicoya Peninsula are large due to the short distance between the source and stations.

817
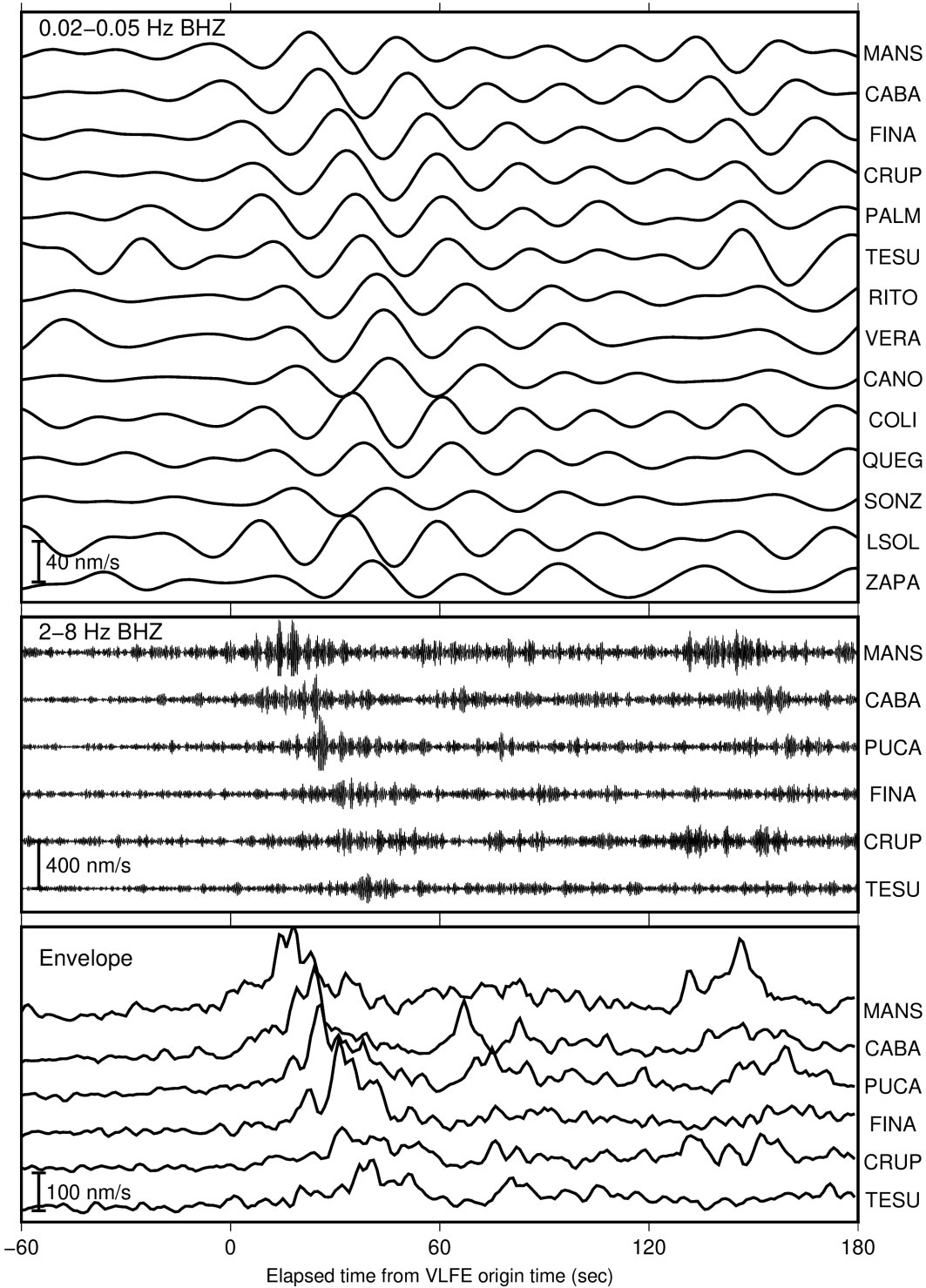
Figure 3. Example of waveforms of a VLFE and the corresponding tremor located at 85.8°W and 9.4°N (shown by a red beachball in Figure 2a) in the frequency range of 0.02–0.05 Hz and 2–8 Hz, and smoothed root-mean-square envelope in the frequency range of 2–8 Hz. Seismograms are shown from the origin time of the VLFE, 03:53:47 (UTC), August 10, 2005.

822
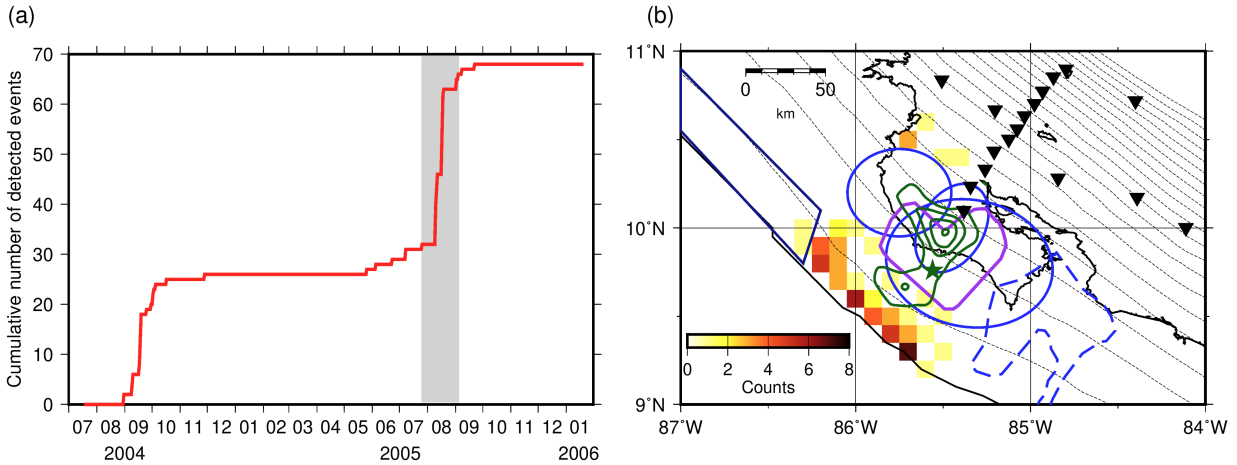
Figure 4. (a) Cumulative number of the VLFEs from July 2004 to January 2006. Gray shading shows the period of the 2005 SSE (Jiang et al., 2012). (b) Distribution of the number of detected events at each virtual source. Blue ellipses and polygons, dark blue quadrangle, inverted triangles, black line, the purple polygon, and dashed contours are the same as in Figure 1.

827
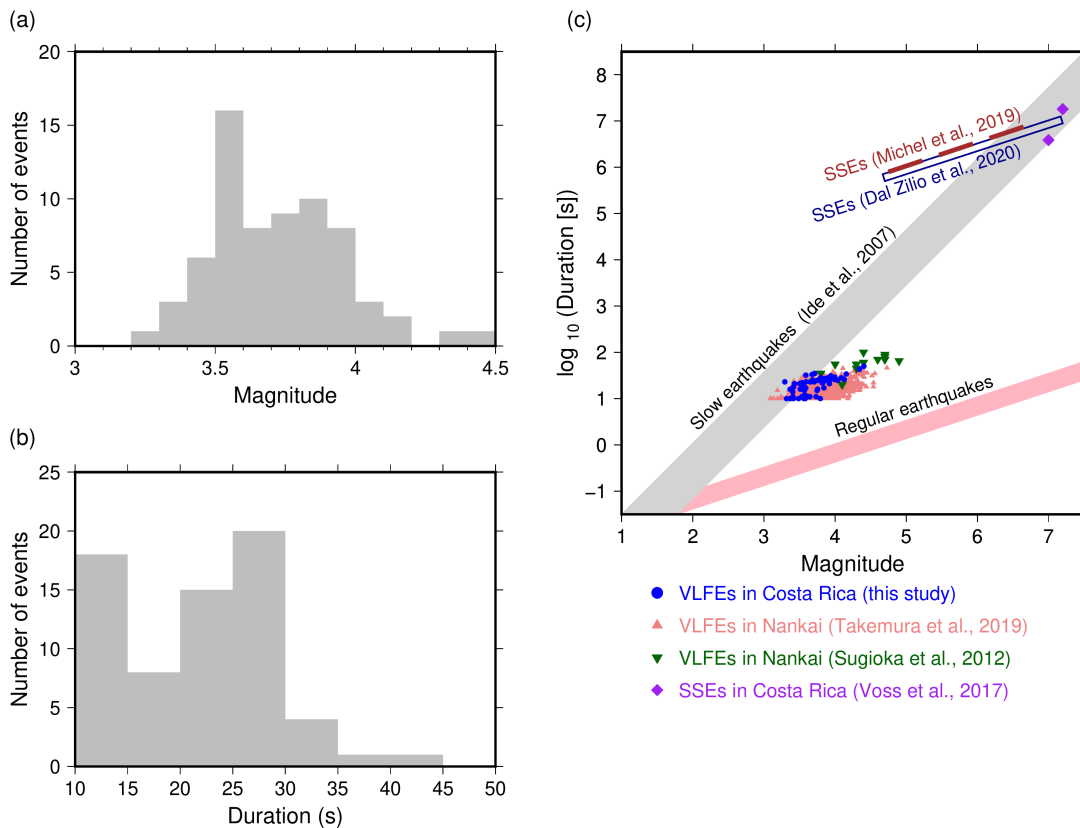
Figure 5. Distribution of (a) magnitudes and (b) source durations of VLFEs. (c) Relationship between durations and magnitudes of slow earthquakes. Gray and pink shadings show the ranges of the scaling law for slow and regular earthquakes by Ide et al. (2007), respectively. Brown dashed

831 line and dark blue rectangle show the range of the scaling law for SSEs suggested by Michel et al.
832 (2019) and Dal Zilio et al. (2020), respectively. Blue dots indicate the relationship between source
833 durations and magnitudes of VLFEs located in this study. Green inverted triangles and pink
834 triangles indicate the relationship between source durations and magnitudes of VLFEs estimated
835 by Sugioka et al. (2012) and Takemura et al. (2019), respectively. Purple diamonds represent the
836 relationship between durations and magnitudes of SSEs in Costa Rica (Voss et al., 2017).
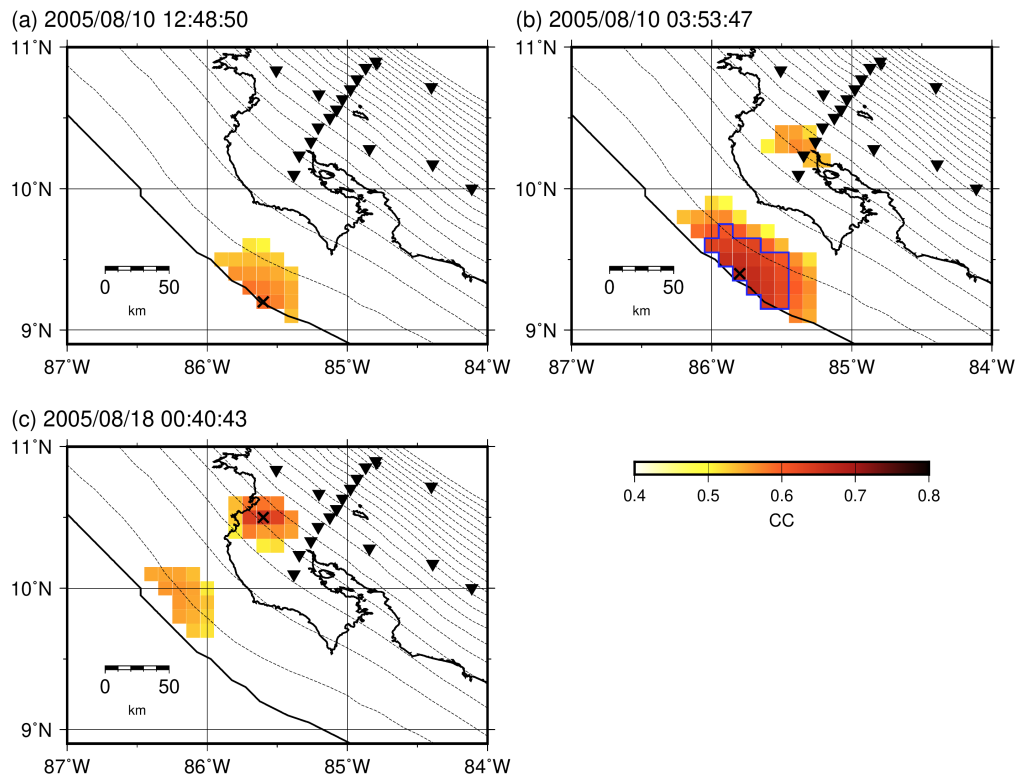
837

838 **Figure 6.** Examples of CC distributions of (a) an event which has large CCs only in updip grids,
839 (b) an event which has large CCs both in updip and downdip grids but is located in an updip grid,
840 and (c) an event which has large CCs both in updip and downdip grids but is located in a downdip
841 grid. Cross mark in each map indicates the epicenter of the VLFE. Inverted triangles, black line,
842 and dashed contours are the same as in Figure 1. The blue polygon in (b) indicates the grids whose
843 CC are more than 0.9 times of the maximum CC.
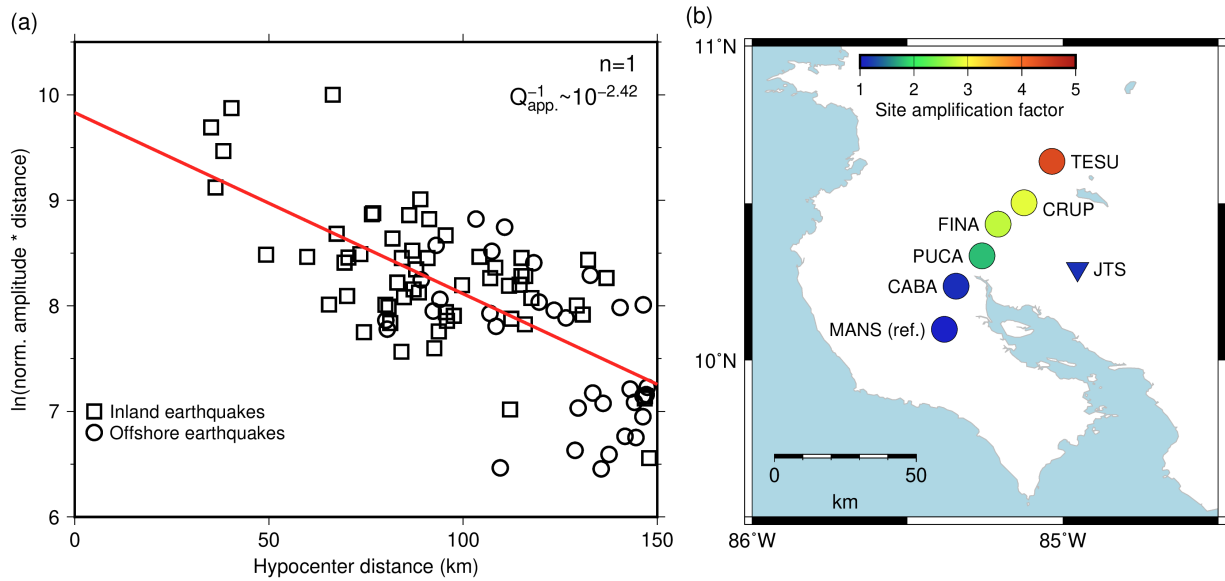
844

845 **Figure 7.** (a) Relationship between logarithm of coda-normalized maximum *S*-wave amplitudes
846 and hypocentral distances. To eliminate effects of geometrical spreading of *S*-wave, coda-
847 nomadized *S*-wave amplitudes were multiplied by their hypocentral distance. Red line shows the
848 regression line using Equation (2). (b) Site amplification factors relative to MANS based on
849 relative coda amplitude measurements.

850
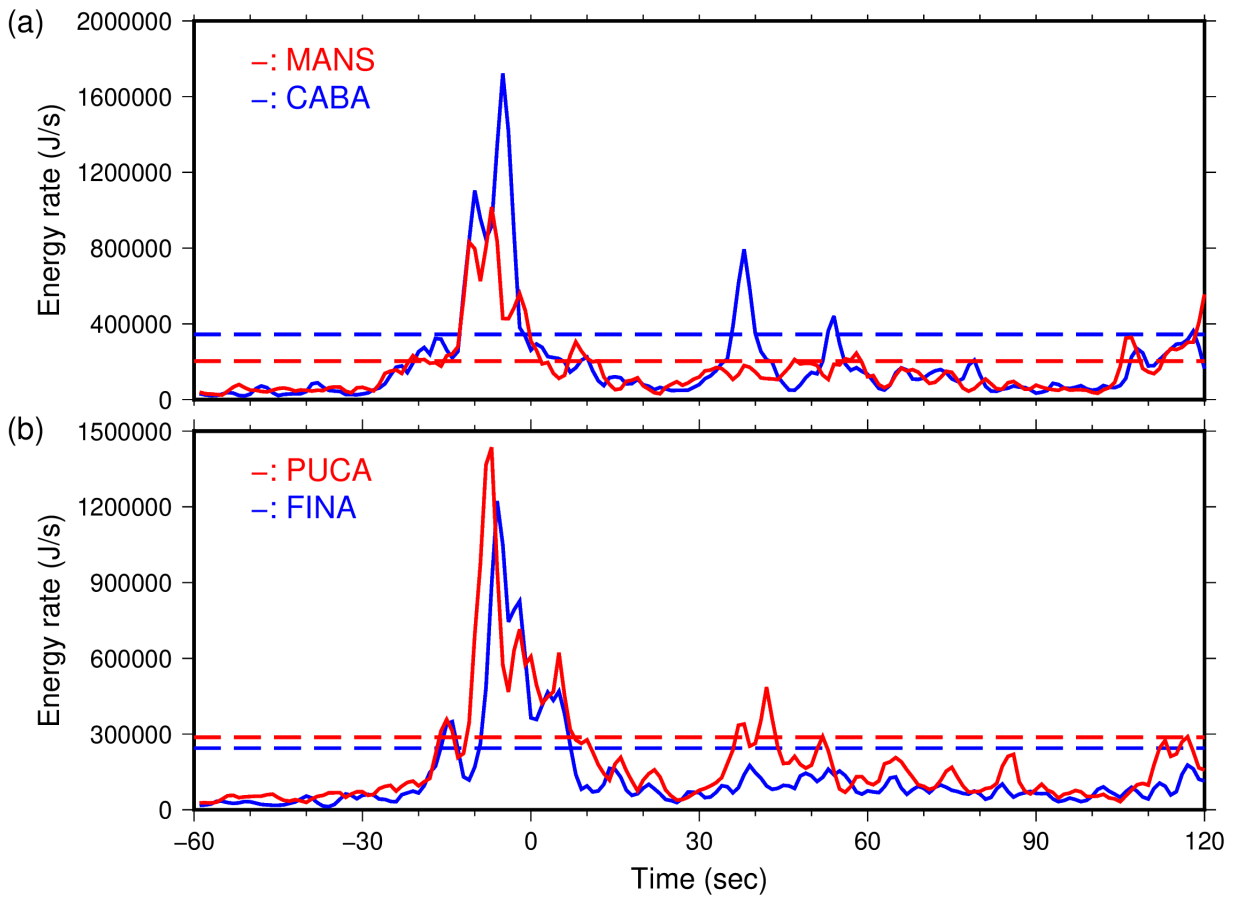
Figure 8. Temporal changes of energy rate functions of a tremor in (a) MANS and CABA and (b) PUCA and FINA. The corresponding VLFE occurs on 03:53:47 (UTC), August 10, 2012. Dashed lines indicate the threshold, which is set as 20% of the maximum value of the energy rate functions.

854
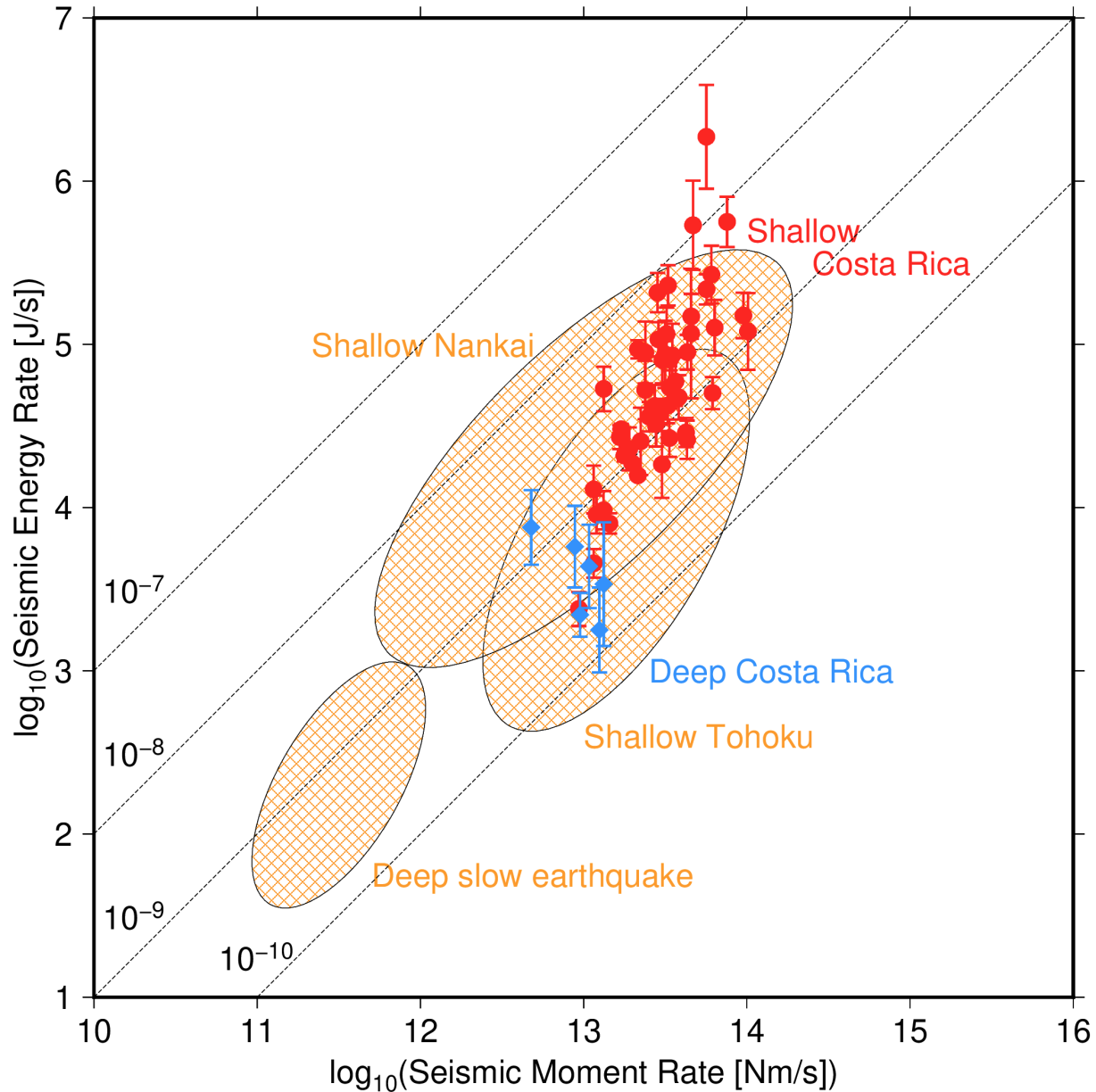
Figure 9. Relationship between seismic moment rates of VLFEs and seismic energy rates of tremors estimated in this study. Red circles and blue diamonds show the events of updip and downdip regions, respectively. Dashed lines show scaled energies of 10^{-7}, 10^{-8}, 10^{-9}, and 10^{-10}. Orange shadings show the relationships between seismic moment rates of VLFEs and seismic moment rates of tremors of shallow slow earthquakes in the Nankai (Yabe et al., 2019) and Tohoku subduction zones (Yabe et al., 2021), and deep slow earthquakes in southwest Japan (Ide & Yabe, 2014), Cascadia (Ide, 2016), and Mexico (Ide & Maury, 2018). We note that scaled energies of shallow slow earthquakes were estimated for individual events, whereas those of deep slow earthquakes were estimated for stacked events.

864
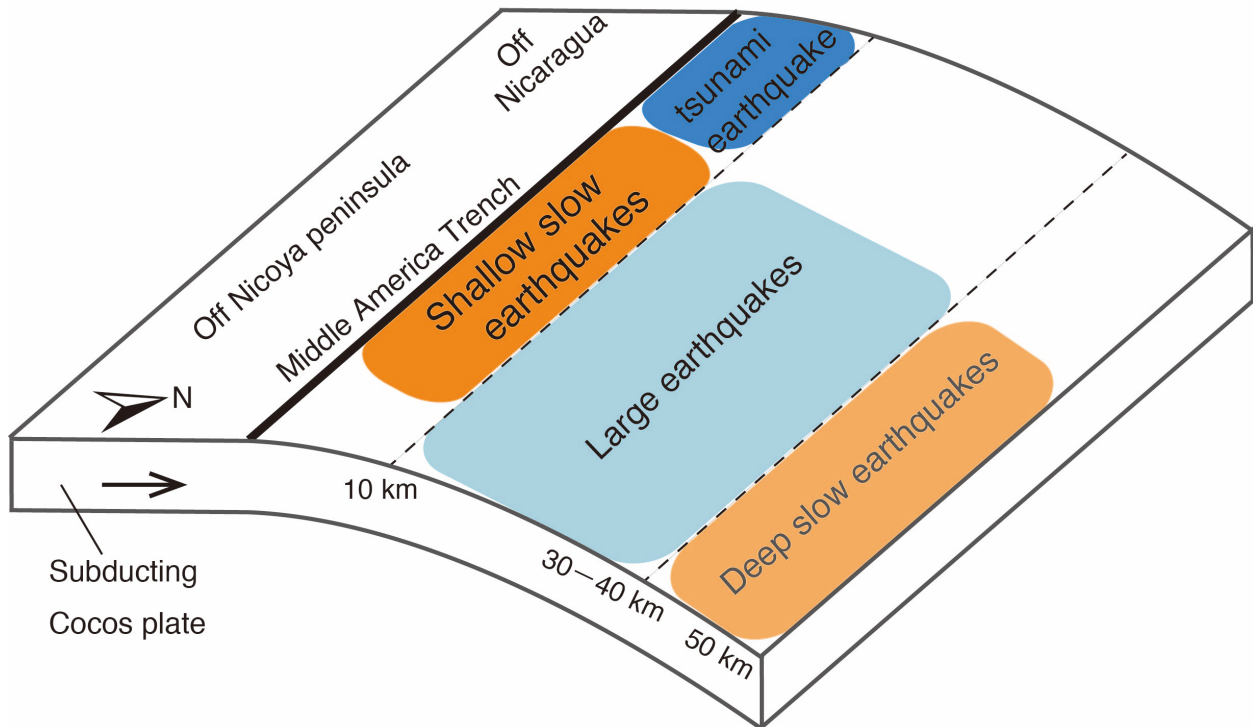
Figure 10. A schematic illustration showing the interpretation of distributions of slow, tsunami, and large regular earthquakes in the Central American subduction zone. The areas of large earthquakes, the 1992 tsunami earthquake, and deep slow earthquakes are referred from Yue et al. (2013), Satake (1994), and Outerbridge et al. (2010), respectively.

869